Simulation of Sinusoidal Diffuse Scattering Loci in the Nonstoichiometric $B8$-Type Alloy Phases $A_{1+x}B$, A = (Co, Ni), B = (Ge, Sn)

Andrew G. Christy[*,1] and Ann-Kristin Larsson[*,†]

Research School of Chemistry, Australian National University, G.P.O. Box 414, Canberra, ACT 2601, Australia; and †Structural Chemistry, Arrhenius Laboratory, Stockholm University, 10691 Stockholm, Sweden

The alloys $(Co, Ni)_{1+x}(Ge, Sn)$ form a range of superstructures in which one $[1\bar{1}0]$ repeat of the hexagonal $B8$ substructure is preserved. Less well-ordered phases also occur in which continuous sinusoidal loci of diffuse scattering are observed trending parallel to c*. The curves can be modeled as cosine waves with maximum k at l = even and minimum k at l = odd. The shape of the curves vary with composition and annealing temperature. Computer simulation was used to generate two-dimensional projections of real-space occupancy patterns that produced similar diffraction patterns. The synthesized real-space arrays were characterized by sets of correlation coefficients. A Monte Carlo algorithm was then used to find sets of two-body interaction energies for which these structures lay at an energy minimum. Good fits between calculated and experimental diffraction patterns were found in all cases. The fitted interaction energies were mainly positive, implying that most two-body interactions were repulsive between sites of like occupancy. Magnitudes were significant out to third-nearest neighboring interstitial sites. The magnitudes tended to be largest near $x = 0.5$. Additional variations of both interaction energies and resulting correlations with composition and annealing temperature are discussed. It is shown that the double-locus diffraction pattern observed for the Ni–Ge system is not necessarily produced by a mechanical mixture of two structures, but can correspond to a single phase. Interactions E_{ij} out to nth nearest neighbors include a larger number of symmetrically distinct $\langle i, j \rangle$ terms than the corresponding $\langle u, v, w \rangle$ terms in three dimensions, implying that only approximate three-dimensional energies can be obtained by fitting from the energies of this study. Mutual frustration of repulsive interactions on the interstitial sublattice, which has a large number of triangularly connected neighbors, is responsible for both breaking the hexagonal symmetry of the sublattice and the failure to form structures giving conventional "spot" diffraction patterns. © 1998 Academic Press

INTRODUCTION

The alloys $(Co, Ni)_{1+x}(Ge, Sn)$ are members of a large group of compounds which are structurally intermediate between NiAs and Ni_2In. The ideal end-member structures have hexagonal unit cells of similar dimensions ($a \approx 4$ Å, $c \approx 5$ Å). The space group is $P6_3/mmc$ for both. The nontransition metals B are at $\pm [\frac{2}{3}, \frac{1}{2}, \frac{1}{4}]$, forming a hexagonal eutactic array. The transition metals in the NiAs structure occupy A sites at $[0, 0, 0]$ and $0, 0, \frac{1}{2}$). In Ni_2In, an additional set of sites A' are occupied at $\mathbf{c}/2$ relative to the B atoms. These sites are on average partially occupied for intermediate compositions. Ordering of the transition metal atoms in excess of $1:1$ stoichiometry leads to formation of a variety of superstructures, due to different occupancy patterns in the A' sites. The experimental data and structural models are discussed in detail elsewhere (1–5). Furthermore, short-range order without long-range order in some of the compounds gives rise to diffraction patterns in which distinctive sinusoidal diffuse streaks are observed trending parallel to the hexagonal $\mathbf{c}$* axis of the substructure (4, 6). The sharp superstructure spots of the commensurate phases lie on or near the positions of such streaks for disordered phases of similar composition. A feature of these compounds, as well as the related $Cu_{1+x}Sn$, which simplifies description and modeling of the ordering patterns in that one $[1\bar{1}0]$ repeat of the substructure is preserved as a lattice translation of the superstructures. The structure may be projected down this vector without loss of information and the ordering treated as a two-dimensional problem. In this projection, the A' sites appear as a rectangular grid with projected repeats $[110]/2$ and $\mathbf{c}/2$ relative to the $B8$ subcell. The corresponding electron diffraction patterns show a rectangular net of Bragg reflections with $00.2l$ and $kk0$ along the principal axes.

In an earlier paper (5), we showed that the atom distributions for the ordered superstructures can be generated as minimum-energy configurations for appropriate combinations of two-body interactions between first- and

[1]To whom correspondence should be addressed. E-mail: christy@rsc.anu.edu.au.

second-nearest neighbors on the projected A' sublattice. Interaction energies were used to determine favorability of atom-vacancy swaps on a computer simulation of the lattice, and potential swaps at random locations were examined until little further change in the overall energy resulted. This Monte Carlo strategy resulted in a real space pattern of occupied and vacant sites from which a diffraction pattern was calculated. Appropriate interaction energies were found that could reproduce every known commensurate structure. Furthermore, it was found possible to calculate the change in structure with composition for fixed interaction energies, assess the change in interaction energies with composition for an experimentally determined sequence of structures in a real system, and to predict the occurrence of two-phase regions. We also found some combinations of interaction energies that gave rise to continuous, sinusoidal loci of diffuse scattering in reciprocal space. Such behavior is observed in the Ni–Sn and Co–(Ge,Sn) systems experimentally. The streaks trend parallel to $\mathbf{c}^*$, vary systematically in both amplitude and mean k value, and may be either uniform in intensity along $\mathbf{c}^*$ or condensed at particular values of l. In the Ni–Ge system, double streaks have been observed.

In this paper, we address the following problems.

(i) What are the real-space occupancy distributions that give rise to these sinusoidal patterns? How do the correlations that describe them vary between systems, with composition and with temperature?

(ii) Do the sinusoidal-locus diffraction patterns correspond to potentially stable ordering patterns? In other words, do there exist sets of interaction energies E_{ij} for which the minimum-energy atom-vacancy distribution gives these patterns? How do these parameters vary between samples?

Only occupational order–disorder is considered at this stage, since this level of information is sufficient to reproduce the major features of the diffraction patterns. However, the presence of some systematic displacement off mean positions is indicated by a slight "size effect" visible in the diffraction patterns (see Results section and Fig. 1).

METHODOLOGY

The partially ordered rectangular nets of both this paper and Ref. (5) have associated with them two qualitatively related but quantitatively different sets of two-body energies, which we call E_{ij} and C_{ij}. The subscripts i and j are the components of a vector between two points in the lattice, in units of $a/2$ and $c/2$, respectively. The energies E_{ij} are two-body interaction energies used to generate a partially ordered arrangement from a random arrangement using the Monte Carlo algorithm outlined above. The energies C_{ij} are descriptive rather than prescriptive and express the two-body correlations in a given atomic distribution. If signifi-

cant in magnitude ($> 0.5\,\mathrm{kT}$), both are usually of the same sign and of comparable magnitude, despite their nonidenticality.

The energies C_{ij} are calculated as $-(\ln K)$, where K is the effective equilibrium constant $4(N_{VV}N_{OO})/(N_{VO})^2$ for the exchange reaction

$$\mathrm{VV} + \mathrm{OO} = \mathrm{VO} + \mathrm{OV}.$$
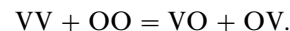
Here, VV corresponds to a pair of vacant sites separated by the vector $[i,j]$, OO is a pair of occupied sites separated by the same vector, and so on. N_{VV} is the proportion of vacant–vacant site pairs, N_{OO} is that of occupied pairs, and N_{VO} is that of vacant–occupied pairs at $\pm(i, \pm j)$ on the virtual lattice. C_{ij} varies qualitatively in the same fashion as the dimensionless Warren short-range order parameter α_{ij} (7, 8), but with reversed sign since positive C_{ij} corresponds to unfavorable vacancy–occupied site interactions. The relationship is not linear, as can be seen from the definition of α_{ij}

$$\alpha_{ij} = \langle s_i s_j \rangle / x(1-x),$$

where x is the proportion of occupied sites, and s_i, s_j are spinlike variables whose value is $(1-x)$ for an occupied site and $-x$ for a vacant site (8–10). The expression above multiplies out as

$$\alpha_{ij} = \{N_{OO}x^2 - N_{VO}x + (1-x) + N_{VV}(1-x)^2\}/$$
$$\{x(1-x)(N_{VV} + N_{VO} + N_{OO})\}.$$

Since $(N_V + N_{VO} + N_{OO})$ is normalized equal to 1, and x is equal to $(N_{OO} + \frac{1}{2}N_{VO})$, this becomes

$$N_{OO}N_{VV}^2 + N_{VV}N_{OO}N_{VO} - \frac{1}{4}N_{OO}N_{VO}^2 - \frac{1}{4}N_{VV}N_{VO}^2$$
$$- \frac{1}{4}N_{VO}^3 + N_{VV}N_{OO}^2 = N_{OO}N_{VV} - \frac{1}{4}N_{VO}^2.$$

In other words, α_{ij} is the difference between the quantities $N_{VV}N_{OO}$ and $\frac{1}{4}N_{VO}^2$, whereas $\exp(-C_{ij})$ is the ratio of these two quantities. One of the parameters α_{ij} or C_{ij} is always calculable from the other, since knowledge of the composition x and the other type of order parameter is sufficient to calculate N_{VV}, N_{VO}, and N_{OO} as proportions of the total number of sites. Specifically,

$$N_{VO,ij} = \{1 - \sqrt{1 - 4x(1-x)(1-K_{ij})}\}/(1 - K_{ij})$$

where $K_{ij} = \exp(-C_{ij}) \neq 1$. For $K_{ij} = 1$, $N_{VO} = 2x(1-x)$. In this study, C_{ij} is preferred since it is in the same units as the prescriptive interaction energies E_{ij} and is of similar magnitude. The significance of small changes in C_{ij} is therefore easier to assess, and it provides a useful set of initial trial

values for E_{ij}. Furthermore, whereas α_{ij} can take only a limited range of values for a given x, this is not true of C_{ij}. For $x \leq 0.5$, the maximum positive correlation corresponds to $N_{VV} = (1 - x)$, $N_{OO} = x$, $N_{VO} = 0$, that is, macroscopic exsolution of vacant and maximally occupied structures. The corresponding $\alpha_{ij} = x(1 - x)$, and $C_{ij} = -\infty$. Conversely, the most negative possible correlation corresponds to maximal dispersal of the minority component through the structure. If the structural topology is such that there are no odd-order closed circuits, as is the case for this study, then the minimum possible correlation corresponds to $N_{VV} = 1 - x$, $N_{OO} = 0$, $N_{VO} = x$, giving $\alpha_{ij} = -x^2/4$. The corresponding c_{ij} is $+\infty$, so there are no constraints on the maximum or minimum values of C_{ij}.

In Ref. (5), sets of E_{ij} appropriate for producing a given diffraction pattern were determined largely by trial and error. Iterative adjustments were made to an initial E_{ij} set until the output C_{ij} and diffraction pattern matched those of the desired structure adequately. This strategy worked well for commensurate and nearly commensurate superstructures for which C_{ij} were easily calculable on paper and were usually either zero or $\pm\infty$, but was not good for simulating the more disordered structures associated with continuous diffuse scattering loci. The C_{ij} for the latter structures cannot be calculated a priori, E_{ij} tend to be smaller in magnitude, and small variations in them make a disproportionately large difference to the ordering pattern obtained. In this paper, a two-stage strategy has been adopted in which C_{ij} for a given diffraction pattern were obtained first. Because of the qualitative similarity between E_{ij} and C_{ij}, the C_{ij} calculated from the modulation wave synthesis were used as trial values of E_{ij}. The latter were then iteratively adjusted in the Monte Carlo fitting program until the output C_{ij} agreed with those of the target diffraction pattern. The two stages are described in detail below.

Modulation Wave Synthesis of Target Patterns

The target C_{ij} values were calculated for a real-space simulation which was generated by modulation wave synthesis. This method for generating real-space patterns that correspond to a specified diffraction pattern has been described in detail by Welberry and Withers (11) and was applied in order to elucidate the real-space configurations producing specific diffraction features (12, 13). As pointed out by Welberry and Withers (14), the resulting real-space distribution is not unique, since the target diffraction pattern contains no information about the phasing of the modulation waves. However, the real-space solutions for different phases differ in their multi body correlations, not in two-body correlations. Therefore, although many different real-space occupancy distributions may produce a given diffraction pattern, the C_{ij} will be the same for all of them.

Van Dyck, de Ridder, and Amelinckx (15, 16) have described an alternative treatment of short-range ordered "transition state" systems that show diffuse scattering along well-defined loci in reciprocal space. They showed that the requirement that diffuse intensity along a locus be non negative causes strong mutual constraint of short-range order parameters, and it confines possible ordering patterns within an n-dimensional domain of existence bounded by $(n - 1)$-dimensional hyperplanes, where n is the number of distinct order parameters considered. Specific loci were related to specific relative weights of different short-range order parameters around a given atom, and hence to preferred local cluster geometries. As it stands, their treatment requires that there is one of the ordering species per lattice point of the average structure, corresponding to diffuse loci which are periodic with the same periodicity in reciprocal space as the average structure. For such systems, it works well. In the $B8$ alloys of the present study, however, the A' atoms are on a hexagonal close-packed array with 2 atoms per cell of the average structure. Strong coupling between the 2 sublattices is evidenced by the fact that the observed sinusoidal loci have period $2c^*$ rather than c^* (cf. Ref. 6). It should be noted that multiple scattering can obscure such long-periodicity behavior in electron diffraction, but this does not occur for the current samples since an $l = $ odd extinction condition applies throughout the plane in which the loci undulate. The cluster approach of (15, 16) cannot be applied to $B8$-type structures without extension of the theory and has not been pursued in the present study, although it is possible that the two-body correlations used to characterize our samples do indeed originate as consequences of multibody cluster interactions (6).

All the sinusoidal diffuse loci in this study had their maximum k values at $l = $ even and their minima of k at $l = $ odd. The variation of k with l could be modeled as (co)sinusoidal in shape with period $2\mathbf{c}^*$, referred to the hexagonal $B8$ subcell, corresponding to the $c/2$ repeat of the projected rectangular A' sublattice. The k coordinate for maximum diffuse intensity as a function of l is therefore given by

$$k = \pm\tfrac{1}{2}((k_0 + k_1) + (k_0 - k_1)\cos\pi l) + N,$$

where k_0 is the maximum k at $l = 0$, k_1 is the minimum k at $l = 1$, and N is an arbitrary integer.

Since quantitative detail in the experimental electron diffraction intensities are likely to be severely perturbed by dynamical effects, only the position of the diffuse scattering in reciprocal space and major qualitative aspects of the intensity distribution were modeled. The following parameters were used to describe the scattering:

(i) the k–l position of the continuous diffuse locus, modeled to be a sinusoidal line with period $2c^*$.

(ii) the locations of any intensive diffuse spots along the streak. Most experimental patterns showed such spots.

The modulation wave synthesis program selected random values of l (between $+1$ and -1) and calculated appropriate k. When l was a uniform variate, a sinusoidal diffuse streak of approximately uniform intensity was obtained. Nonuniform intensity along the line was obtained by making l a Gaussian variate with standard deviation σ; this was used to generate the strong spots centred on specific l values. The majority of experimental diffraction patterns were qualitatively well fitted by a superposition of a uniform line with Gaussian-profile spots of $\sigma = 0.05$–0.10. Note that "uniform" ($\sigma = \infty$) and finite values of σ here refer to the distribution of l. There was a unique value of k calculated for each l, corresponding to zero width of the undulating line for infinite size of modulation wave domain. Since the domains were in practice finite (see below), a definite width of line was obtained in the calculated patterns. Typically, half of the modulation waves were devoted to defining the lines, half to the spots, although the proportions of these were adjustable. The l value at which the spots were centered was usually $l = \pm 0.5$, 1.5, but in some cases was $l =$ integral. The program included these options.

In order to synthesize the real-space modulation function, domains of a fixed area were selected from the virtual lattice, and fixed-amplitude cosine waves of the appropriate wavevector were added to the total real-space modulation function within that domain. In this study, the domains were approximately circular. The positions of the domain centers were random in both y and z, and they were continuous variables rather than discrete. The phases of the waves were therefore random. After a large number of such waves had been summed, the cumulative modulation function was discretized to give the occupancy of each site (0 or 1). This was done by iteratively locating the threshold value of the modulation function such that proportion x of lattice sites had a higher value, where x was the intended composition for the simulation. Once a lattice of binary occupancy variables was obtained, the corresponding C_{ij} could be calculated, and the program DIFFUSE (17) was used to verify that the diffraction pattern corresponding to the discrete real-space array was indeed close to that originally specified.

One aspect of this simulation that requires comment is the number of modulation waves that are superposed in order to produce the real-space pattern. Clearly, use of too few waves would result in a very inhomogenous real-space occupancy pattern, whereas use of too many would gain little in data quality while wasting computer time. Since the simulated lattice was a 500×500 grid, the use of 1000 modulation domains with area $\pi \times 20^2$ each resulted in about 5 waves being superposed at each lattice point. In order to establish the optimal number of waves, test simulations of a target pattern were run ranging from average of 1.7 waves per lattice point (300 waves total) to 5000 waves per lattice point (1,000,000 waves total). It was found that

the variation of C_{ij} values obtained as a function of number of waves was less than ± 0.05 kT for all except two C_{ij} of large magnitude, provided the total number of waves was over 1000. For most of the simulations of this study, 20,000 waves of radius 20 were applied to the virtual lattice.

Fitting of E_{ij} Values to C_{ij}

The modulation wave synthesis produced a distribution of occupied and vacant sites in real space which gave a diffraction pattern resembling that of the sample. The occupancy pattern was characterized in terms of a set of C_{ij} values, which are convertible into Warren–Cowley short-range order parameters if the composition is known. The second stage of the modeling process in this study was to obtain for each diffraction pattern, if possible, a set of two-body interaction energies E_{ij} giving rise to a similarly correlated real space structure as a minimum-energy configuration.

As stated above, interaction energies E_{ij} produce equilibrium configurations of vacancies and occupied sites whose C_{ij} are not numerically equal to E_{ij} but which vary in the same qualitative fashion. The main reason for the lack of numerical agreement is that a given E_{ij} interaction results in contributions to several C_{ij} correlations. For example, positive E_{10} will tend to produce positive C_{10} (avoidance of similar occupancy in adjacent sites along **b**) but through self-coupling will also make negative contributions to C_{20}, positive to C_{30} and so on. Away from the principal axes, the situation is more complex since the energy E_{ij} operates between points separated by vectors $[i, j]$, $[i, -j]$, $[-i, j]$, and $[-i, -j]$, all related by the symmetry of the projected sublattice. Correlations C_{UV} are affected for any $[u, v]$ that can be constructed as sums of integral multiples of these vectors. Furthermore, this is generally true for any pair of E_{ij} which are not related by symmetry. For example, E_{12} alone affects C_{ij} with $i = 2m$, $j = 4n$ and with $i = 2m + 1$, $j = 4n + 2$ (m, n integers). E_{11} affects C_{ij} with $i = 2m$, $j = 2n$ and with $i = 2m + 1$, $j = 2n + 1$. If both are nonzero, all C_{ij} are affected, since any i and j can be made out of a suitable combination of multiples of $[1, 1]$ and $[1, 2]$. It is impossible to derive analytically the E_{ij} that correspond to a given set of C_{ij} values.

For this study, it was necessary to start with a trial set of E_{ij}, obtain an equilibrated configuration of vacancies and occupied sites, calculate the corresponding C_{ij}, and adjust E_{ij} iteratively until a good fit between calculated C_{ij} and their target values was achieved. The program used to do this was a modification of that used in (5) adapted to include longer-range interaction terms out to $i = 6$, $j = 4$. It will be seen below that these longer range terms are necessary to define the fine detail in the more complicated diffraction patterns.

The program used to obtain E_{ij} started with trial values that were usually the C_{ij} set obtained from the modulation wave synthesis. After the Monte Carlo routine had examined every site in the real space array an average of once for the possibility of exchange with another site, the C_{ij} were calculated for the occupation pattern so far, and the E_{ij} values adjusted according to the difference between actual and target C_{ij}. Best fits, characterized by the root-mean-square deviation between fitted and target C_{ij} values for all $[i, j]$ where the E_{ij} was a refineable parameter, were (with one exception) better than 0.1 kT and in some cases they were better than 0.01 kT. Usually, 20–60 cycles of iteration were needed until this level of agreement was reached, and the fit did not improve significantly beyond the best obtained at that stage.

The maximum magnitude of E_{ij} permitted was set at ± 5.0 kT, as in (5), given the limited size of the real space array. A magnitude this large for C_{ij} corresponds to a maximum N_{vo} of only 0.0759 at $x = 0.5$. If N_{vo} is small, then very small changes in it result in large changes to C_{ij}, so the values obtained become less precise. In any case, few C_{ij} obtained from the modulation wave synthesis were found to be as big as ± 5 kT. This limiting range was chosen for the E_{ij} values given that they were comparable in size to the corresponding C_{ij}, and because it was found that allowing very large interaction energies led to them dominating the fitting process and prevented good fits for C_{ij} associated with smaller E_{ij}.

EXPERIMENTAL DIFFRACTION PATTERNS

A brief description of the diffuse lines seen in the (Co, Ni)–(Sn, Ge) systems is set out below. It should be noted that all indices were obtained by direct measurement from electron diffraction patterns and are only approximate. The width of the lines and their faintness at some important values of l imply an error in measurement of k of at least ± 0.02. Any additional diffuse structure was very faint. The lines modeled in this study appear to arise predominantly from occupational short-range order, although a slight modulation of intensity resulting from a size effect was visible in some experimental patterns (Ni–Sn and Co–Ge systems).

The experimental diffraction patterns are described below, along with the details of their modeling in the modulation wave synthesis. Experimental patterns have been published previously for the Sn-bearing systems (6) and the Ni–Ge system (4). The numerical parameters used to define the diffuse lines in the simulations are summarized in Table 1.

Co–Sn System

The simplest undulating diffuse line type was observed in the Co–Sn system, which has a limited solid solution range

TABLE 1
Characteristics of Experimental Systems as Modeled in the Modulation Wave Synthesis

Simulation number	System	x	k_0	k_1	l (spot)	σ
1	Co–Sn	?	0.37	0.24	—	—
2	Ni–Sn	0.34	0.40	0.20	0, 1	0.05
3		0.525	0.37	0.24	0, 1	0.05
4		0.61	0.36	0.28	0, 1	0.05
5	Co–Ge	0.63 (lt)	0.36	0.32	0.5, 1.5	0.05
6		0.63 (ht)	0.36	0.27	0.5, 1.5	0.1
7		0.70 (ht)	0.38	0.26	0.5, 1.5	0.1
8		0.86 (lt)	0.40	0.26	0.5, 1.5	0.1
9a	Ni–Ge	0.70	0.32	0.22	0.5, 1.5	0.1
9b			0.41	0.33	0.5, 1.5	0.1

of $x = 0.38$–0.61 (6, 18, 19). Slowly cooled samples had an ordered superstructure, but those quenched from 1000–1150°C showed continuous diffuse curves (Ref. 6, Fig. 2). The intensity variation along the diffuse lines was only slight, and was not included in the model. The value k ranged from $k_0 = 0.37$ at $l =$ even to $k_1 = 0.24$ at $l =$ odd. The composition of the sample whose diffraction pattern was shown in Ref. (12) was not known exactly but $x \leq 0.5$.

For a given diffraction pattern, the E_{ij} values vary with x, but are symmetrical about $x = 0.5$. Extreme values were therefore fitted for $x = 0.38$ and $x = 0.50$, using the k values measured.

Ni–Sn System

Like the Co–Sn system, continuous diffuse lines were found for samples quenched from high temperature. The form of the sinusoids varied noticeably with composition. At $x = 0.34$, $k_0 = 0.40$ and $k_1 = 0.20$. However, at $x = 0.525$, $k_0 = 0.37$ and $k_1 = 0.24$, and at $x = 0.61$, $k_0 = 0.36$ and $k_1 = 0.28$. Sharp spots ($\sigma = 0.05$) occurred at $l =$ integral (Ref. 6, Fig. 5). These were modeled by using half of the modulation waves to generate the spots (Gaussian-distributed l with $\sigma = 0.05$) and half to contribute to the continuous lines. Real space distributions and diffraction patterns were calculated corresponding to the experimental electron diffraction patterns with $x = 0.34$, 0.525, and 0.61.

The experimental patterns (6) show a slight intensity transfer from lower to higher angle diffuse loci, indicating a size effect similar to that in the Co–Ge system (see below).

Co–Ge System

Experimental electron diffraction patterns for this system have not been published previously and are shown in Fig. 1.
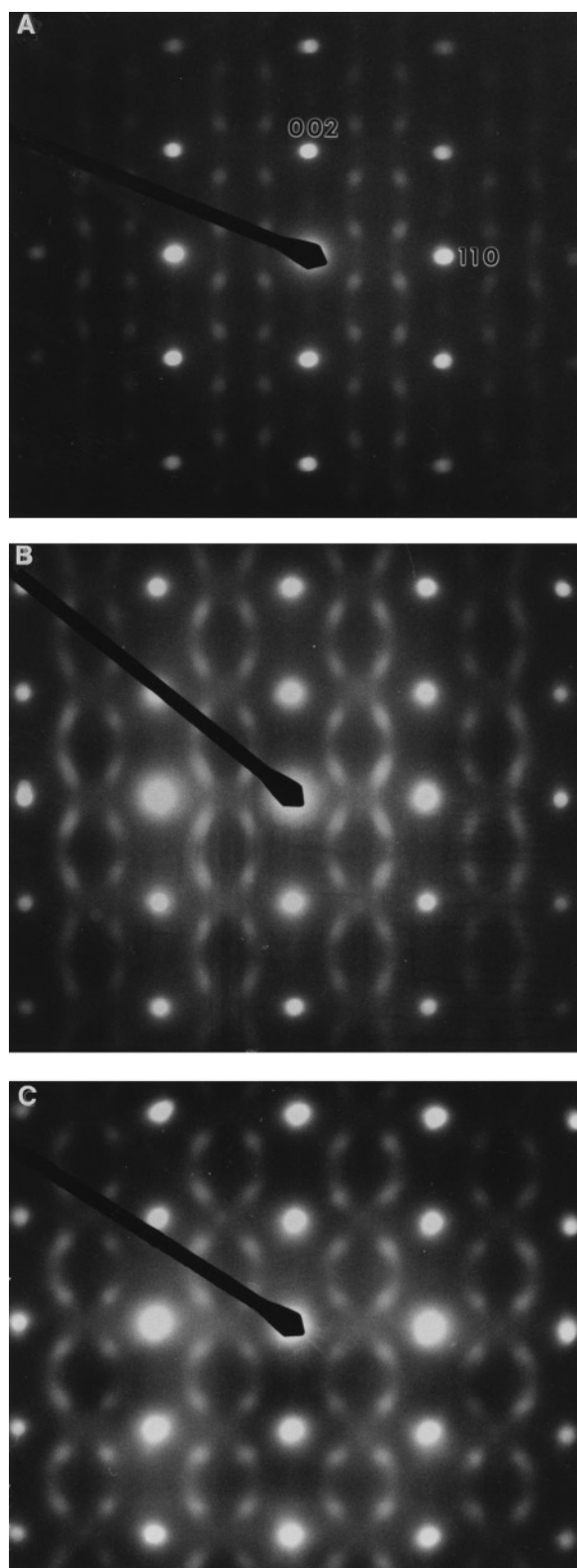
FIG. 1. Experimental electron diffraction patterns for the Co–Ge system. Viewing direction parallel to $[1\bar{1}0]_{BS}$. (a) $x = 0.63$, annealed at 600°C. (b) $x = 0.63$ annealed at 982°C (c) $x = 0.86$, approximately. Cooled from 700°C to 500°C at 10°C/min, then quenched.

In the Co–Ge system, the intensity maxima were at $l = 0.5$ and 1.5 rather than integral l values as seen in the Ni–Sn system. For $x = 0.63$, at the low-x end of the composition range studied, $k_0 = 0.36$, $k_1 = 0.32$ in a sample quenched from 600°C and $k_0 = 0.36$, $k_1 = 0.27$ in a quench from 982°C. The spots in the low-temperature diffraction pattern were somewhat sharper than all other Co–Ge patterns, and σ was set accordingly as 0.05 rather than the usual value 0.1. For $x = 0.70$ quenched from 1200°C, $k_0 = 0.38$ and $k_1 = 0.26$. The highest x sample was inhomogeneous, but the majority phase had estimated $x = 0.86$. This sample was cooled at 10°C/min over the temperature range 700–500°C and then quenched. Nevertheless, the spots in the diffraction pattern were as broad as those of the high-temperature samples. For this sample, $k_1 = 0.26$, and $k_0 = 0.40$ if it is assumed that there are sinusoidal loci similar to those for all the other samples. However, the loci appear to merge in broad patches of diffuse intensity at $l = 2n$, and this sample appears to be atypical.

The last three patterns suggest that k_0 gradually increases with x. The low-temperature low-x pattern is the only one for which $k_1 \neq 0.26$–0.27 in this system. Fits were calculated for $x = 0.63$ quenched from 600°C and from 982°C, and also the pattern for $x = 0.86$. The three corresponding diffraction patterns span the range of behavior observed in this system.

A slight *atomic size effect* (7, 10, 12) is noticeable in the diffraction patterns of Fig. 1b and 1c, in that the intensities of the lines at $-0.5 < k < 0.5$ are systematically lower than those of their higher angle counterparts at $0.5 < |k| < 1.0$. This implies that a local expansion of the crystal structure occurs around regions of relatively low mean local scattering factor, and hence is consistent with a slight relaxation of atoms away from vacant A' sites and toward occupied ones. Note that this distortion is in the opposite sense to that noted in the structure refinement of η'-Cu$_6$Sn$_5$ (2, 5), where there is overall expansion around the occupied sites.

Ni–Ge System

This system has the widest composition range out of the four considered in this paper. Many commensurate superstructures have been characterized, which are discussed in detail elsewhere (4, 5). Undulatory diffuse loci were only observed at the high-x end of the composition range ($x > 0.7$). The unusual feature of these samples was the occurrence of two sets of curved loci, one at higher k than the other. Spots occurred near $l = 0.5$ for both. The spots were distinctly elongated, so $\sigma = 0.1$ was used. For a sample with $x = 0.70$, the curves had $k_0 = 0.32$ and $k_1 = 0.22$ for the outer, stronger curve and $k_0 = 0.41$, $k_1 = 0.33$ for the inner, weaker curve. The modulation wave synthesis used 25,000 waves for the outer curve and 15,000 for the inner, giving a 5 : 3 intensity ratio. Similar patterns were obtained
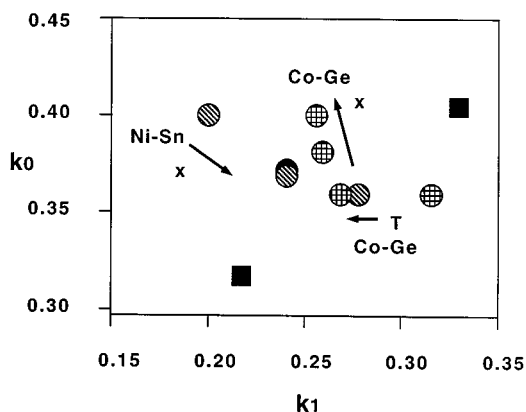
FIG. 2. Plot of k_0 against k_1 for the samples of Table 1. Black circle indicates Co–Sn system. Shaded circles Ni–Sn, cross-hatched circles Co–Ge. Effect of varying x and T shown for the latter two cases. Black squares indicate the two lines for the Ni–Ge system.

experimentally for higher x values up to 0.88, but the samples were no longer homogeneous: the appearance of strong spots at $(0, 0, 1)$ and $(0.5, 0.5, 0)$ implied the presence of domains with a commensurate Ni_2Ge superstructure.

The characteristics of nine different patterns as modeled are summarized in Table 1, and the variation of k_1 with k_0 is depicted in Fig. 2. It is apparent that most of the curves lie on a single trend of k_1 increasing as k_0 decreases. The variation with x is in the opposite sense for the Ni–Sn and Co–Ge curves. Note that the two curves coexisting in the $Ni_{1.70}Ge$ diffraction pattern lie on either side of the trend for all the other curves, suggesting that the "normal" single locus in this system is destabilized and disproportionates into a pair on opposite sides of the usual k–l trend.

Close agreement was obtained between the C_{ij} from the modulation wave synthesis and those obtained from the Monte Carlo fitting program in almost all cases. Root-mean-square deviations between the two ranged from 0.007 to 0.034, except for simulation #4 (0.073) and #8 (0.186). The strong diffuse features were very similar in diffraction patterns calculated for the two with the exception of simulation #8, although those from the Monte Carlo distributions tended to have less sharp lines and more faint spurious detail. Nevertheless, the overall intensity distributions in the Monte Carlo patterns closely resembled those of the electron diffraction pattern being modeled. Therefore, the real space distributions and C_{ij} values from the modulation wave synthesis are not considered further, although they constituted a necessary intermediate stage in obtaining the data sets from the Monte Carlo E_{ij} fitting routine, which are discussed in detail below. Note that the fact that it was possible to obtain good matches to the diffraction patterns while refining E_{ij} in the Monte Carlo routine implies that there exists a set of E_{ij} values for which the equilibrium structure gives the target diffraction pattern. It is therefore

possible, although not necessary, that the structure obtained is a thermodynamically stable phase under appropriate conditions.

RESULTS

Portions of the fitted real space occupancy distributions for the Co–Sn system are shown in Fig. 3. Note that the real space figures are analogous to high-resolution transmission electron micrographs in that each pixel represents a column of filled or empty A' sites projected down $[1\,\bar{1}\,0]$. Similar data are shown in Fig. 4 for the Ni–Sn system, and calculated diffraction patterns for the Sn-bearing systems are shown Fig. 5. Real space and reciprocal space patterns are shown in Figs. 6 and 7 for the Co–Ge system, and Figs. 8a and 8b for the Ni–Ge double-line structure.

Note that very small domains of commensurate γ'-Co_3Sn_2 type structure are visible in the real space patterns for the Sn-bearing phases (Figs. 3–4). These appear to be
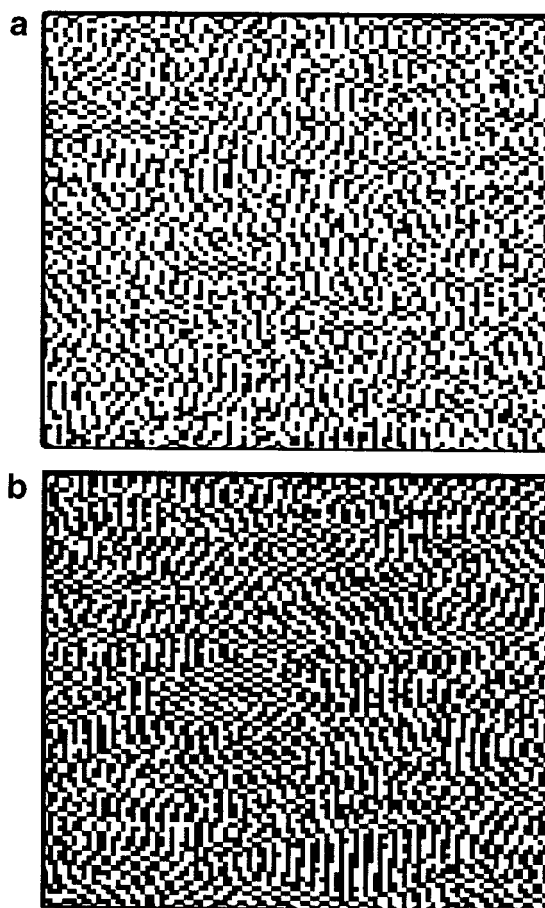

FIG. 3. Real space occupancy patterns for the fits to the Co–Sn diffraction pattern with (a) $x = 0.34$ and (b) $x = 0.5$. The pseudohexagonal **c** axis is vertical. The black and white pixels correspond, respectively, to columns of occupied and vacant sites projected along $[1\bar{1}0]_{B8}$.
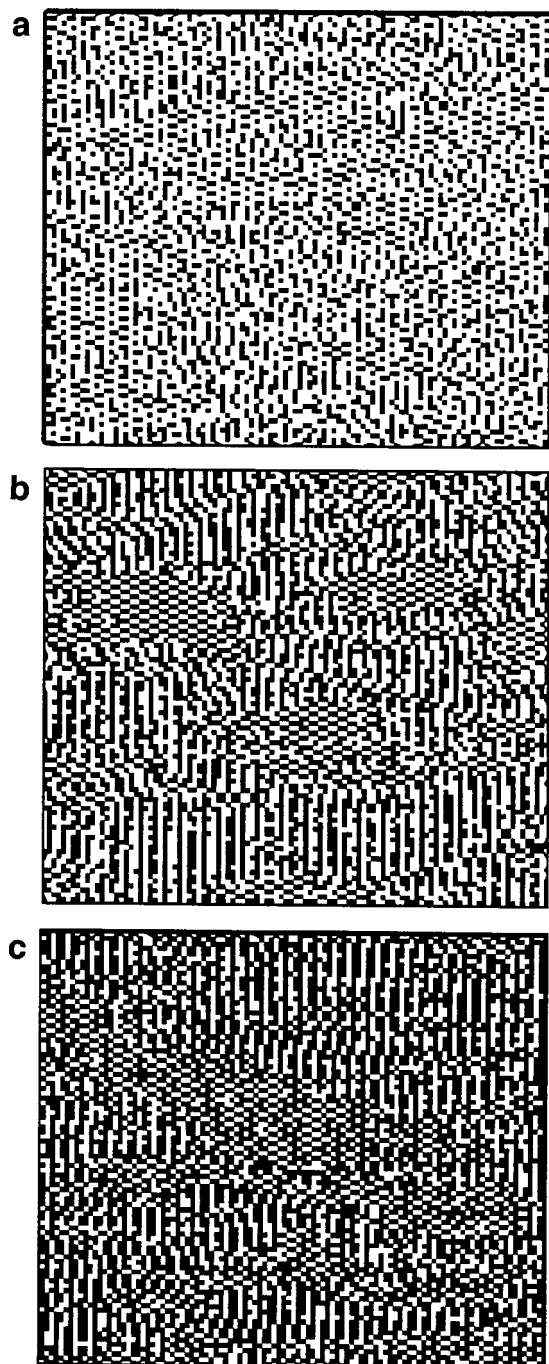
FIG. 4. Real space occupancies for the fits of the Ni–Sn system. (a) $x = 0.34$, (b) $x = 0.525$, (c) $x = 0.61$.

FIG. 5. Calculated diffraction patterns for (a) $Co_{1.38}Sn$, (b) $Ni_{1.34}Sn$, and (c) $Ni_{1.61}Sn$ using the parameters of Table 1. Compare (a) with Ref. (6), Fig. 2 and (b)–(c) with Ref. (6), Fig. 5.

examples of local approximation to ordered superstructures in structures which are generally devoid of long-range translational repetition.

Domains of Co_2Ge composition can be seen in Fig. 6c. It is noteworthy that the corresponding diffraction pattern (Fig. 7c) is by far the worst approximation to the correspond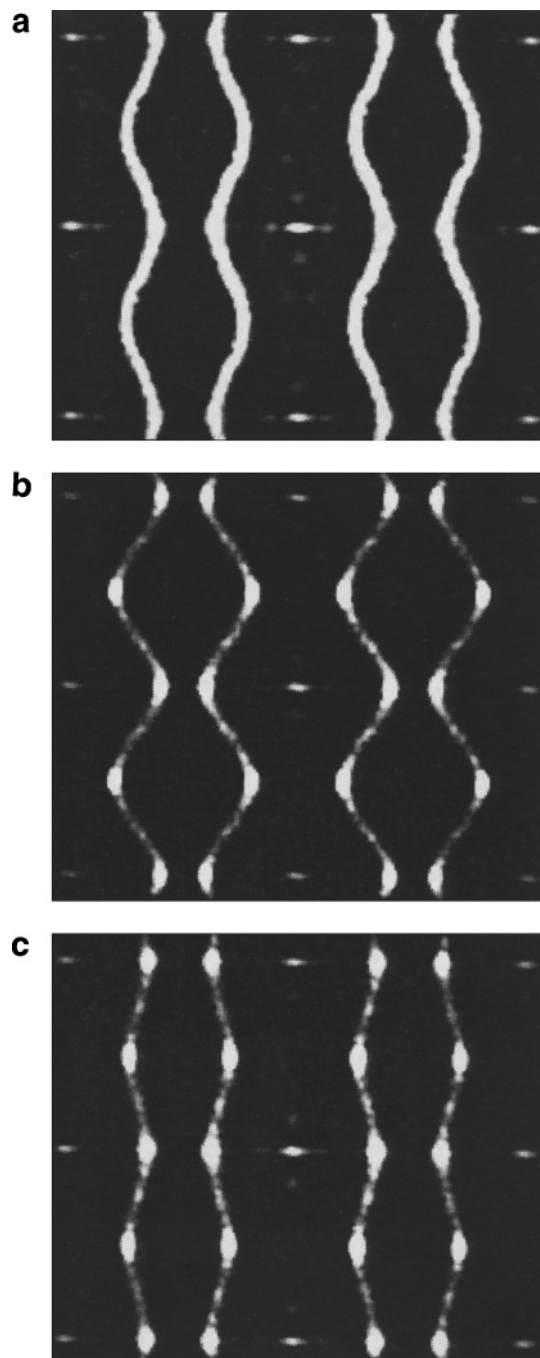ing experimental pattern (Fig. 1c) obtained in this study. The experimental diffuse scattering does not appear to lie on a simple sinusoid with period $2c^*$ for this sample (see discussion below). The match between Fig. 1(a, b) and Fig. 7(a, b) is considerably better, although not as good as those between Fig. 5(a–c) and Fig. 8b and the experimental patterns published previously (6).
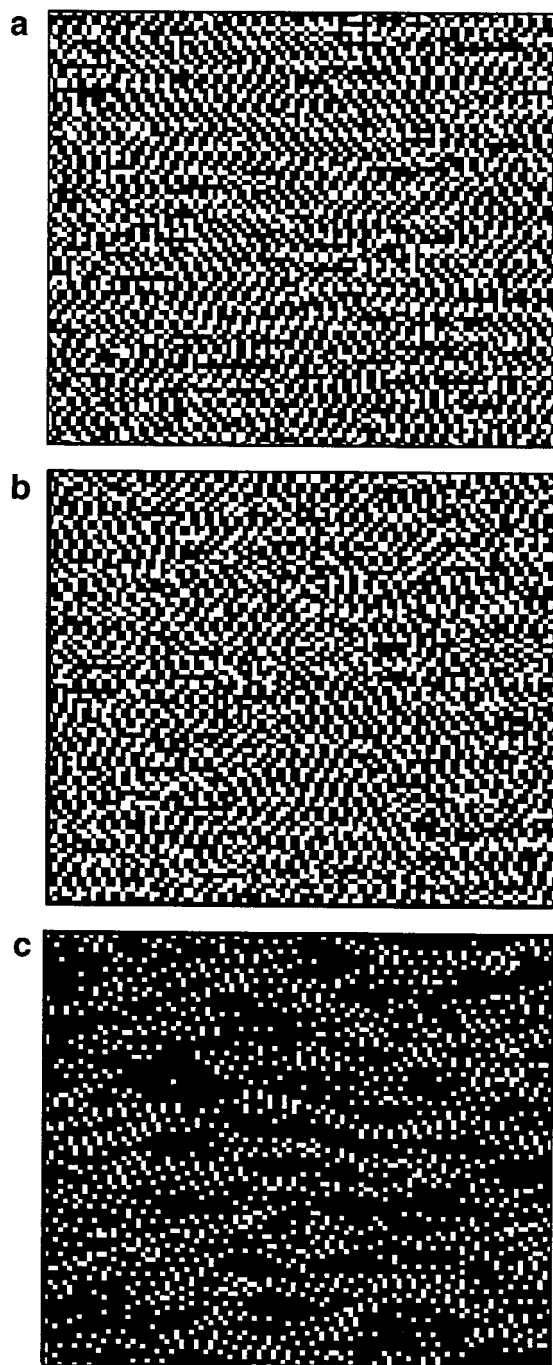
FIG. 6. Real space occupancies for the fits of the Co–Ge system. Black and white reversed relative to Figs. 2 and 3 for clearly, since all $x > 0.5$. (a) $x = 0.63$, low temperature (b) $x = 0.63$, high temperature, (c) $x = 0.86$, approximately.
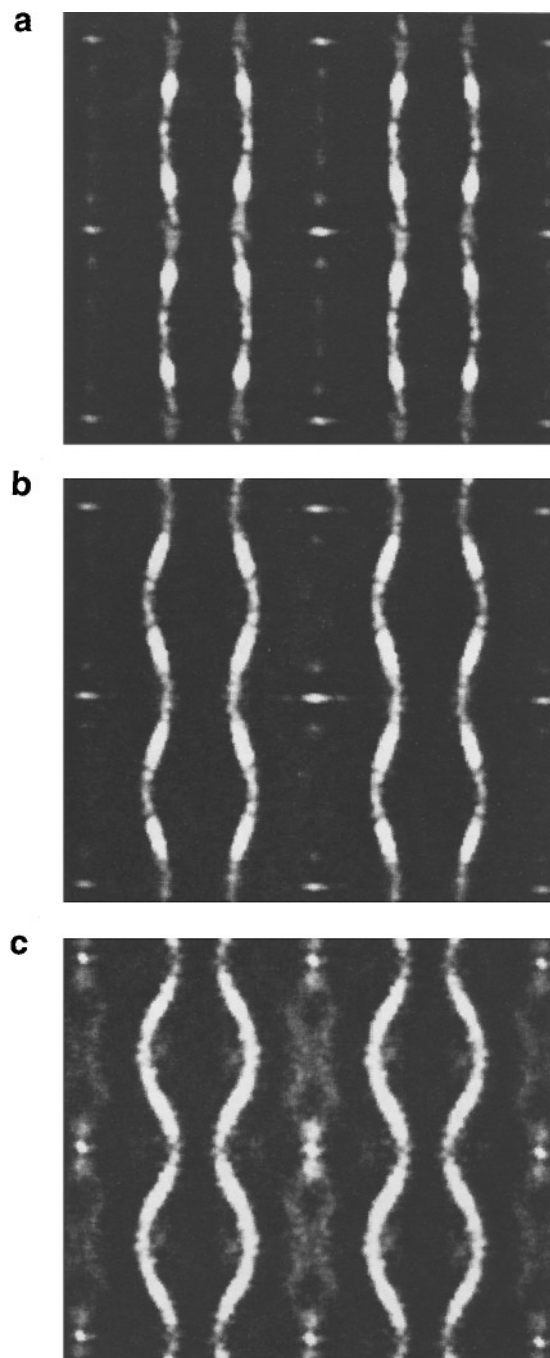

FIG. 7. Calculated diffraction patterns corresponding to the real space distributions of Fig. 6 (simulations #6 to #8), and also to the experimental diffraction patterns of Fig. 1. Note reasonably good agreement with experiment for (a) and (b) but bad agreement for (c).

DISCUSSION

Variation of C_{ij}

The C_{ij} values for the Co–Sn system were characteristic of sinusoidal diffuse lines unmodified by spots or other intensity modulation. The C_{0j} values were all small,

corresponding to poor correlation along the **c** direction in real space and continuous loci of diffuse scattering trending along **c***. Conversely, the C_{i0} values tended to be large in magnitude, implying good correlation in the xy plane in real space and condensation of the diffuse structure normal to **c***. Strongly positive C_{20}, negative C_{30}, and relatively small
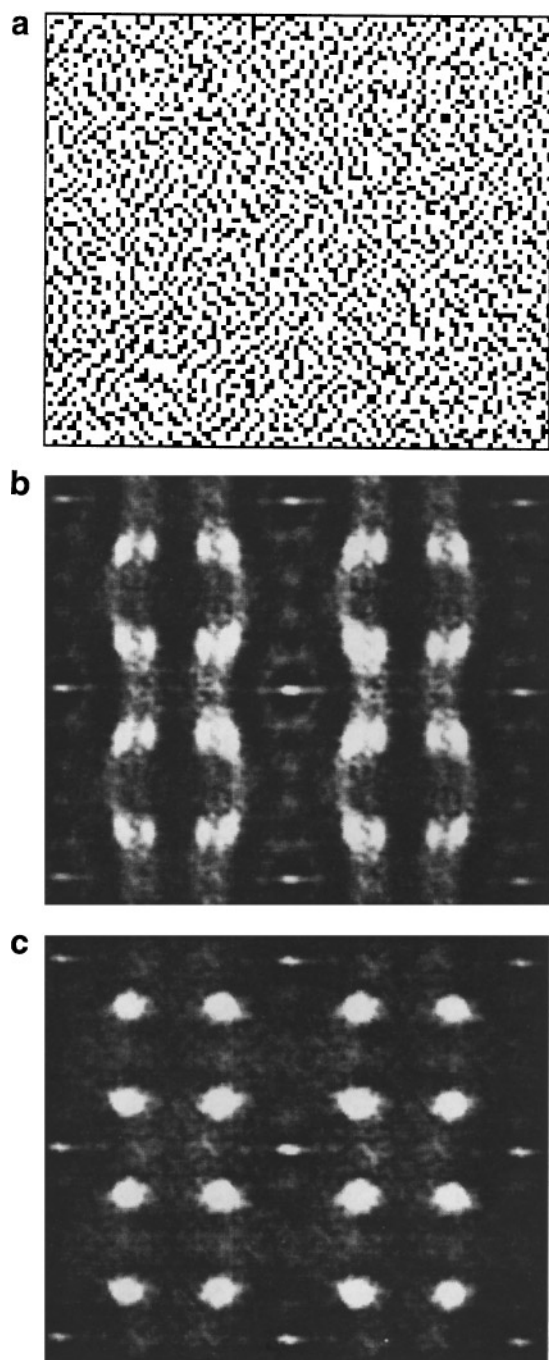
FIG. 8. The $Ni_{1.70}Ge$ "double line" and related structures (a) lattice realization, (b) calculated diffraction pattern, and (c) diffraction pattern for equilibrated structure with $E_{ij} = 0$ for $i = 5,6$. Note poorly defined lines and loss of double-line structure.

negative C_{40} all suggested that the diffuse lines in the diffraction pattern intercept the $l = 0$ line near $(\frac{1}{3} \frac{1}{3} 0)$, approximately consistent with the observed value of $k_0 = 0.37$. Perturbation of the diffuse line away from constant k was implied by the presence of "diagonal" correlations ($i, j \neq 0$)

of significant magnitude. In this case, these were C_{i1} ($i = 1$–6) and C_{25}, particularly. All of the fits obtained in this study showed several significant diagonal correlations, which varied in a complex fashion with the shape of the sinusoidal locus. The overall trends toward more positive and more negative values were similar in the C_{ij} values and the corresponding E_{ij}, but the latter tended to be more positive.

The occurrence of spots on the lines correlated with larger magnitudes for C_{02} and C_{04}, which were either both negative (spots at $l = $ integral positions, as for Ni–Sn) or positive and negative, respectively (spots at $l = $ half-integral, as for the Ge-bearing systems). Corresponding negative and positive deviations occurred in E_{02}, E_{04} relative to the values for E_{01} and E_{03} for all simulations except the poorly fitted #8.

The correlation energies C_{01}, C_{04}, C_{21}, and C_{30} were the only such terms that were negative throughout, implying a tendency toward similar occupancy of sites separated by the corresponding vectors in all systems. Conversely, C_{10}, C_{11}, C_{20}, and C_{41} were always positive. The positive sign of C_{i0} for $i = 1, 2$ and negative sign for $i = 3$ implied avoidance of similar occupancies for immediately adjacent A' in a $(001)_{B8}$ layer of the structure, combined with a preference for the "honeycomb" ordering pattern noted in many of the commensurate structures (1–5). Other correlations varied systematically from system to system. In particular, C_{02} was negative for the Sn-bearing phases and positive for the Ge-bearing phases, consistent with the tendency for spots to appear in the diffraction patterns at $l = $ integral positions in the former and $l = $ half-integral in the latter. C_{23} varied similarly, which is likely to be a consequence of coupling to C_{02} through C_{21}, which was always negative (i.e., positive correlation).

Variation of E_{ij}

The overall pattern of variation for E_{ij} was similar, but with some sign changes for small magnitudes due to the bias toward more positive values mentioned above. In fact, out of 34 such terms, 20 were consistently positive in all simulations. There is an implication that many of the correlations observed indicate the least unfavorable relative positions for like occupancies rather than any attractive interaction as such. The main exception was the E_{30} term, negative except for one Ni–Sn simulation, which supports the idea that there is a definite driving force for honeycomb ordering in the xy plane. E_{51} was also negative except for the Ni–Ge simulation. Interestingly, E_{62} behaved in the opposite fashion, suggesting that these two relatively long-distance (ca. 11 Å) interactions may be important in producing the double-line diffraction pattern in this system. Although long relative to the 4–5 Å shortest A'–A' distances in these materials, such distances are still appreciably shorter than the elastically-mediated interactions known to occur between

plane defects in some oxide systems (20–22), and it seems feasible that interaction between the strain fields around A' substituents and their neighbors over > 10 Å may determine these long-range correlations. The nature of the Ni–Ge phase is discussed in more detail below.

Variation with x

Trends with varying composition within the same system were not obvious. The two simulations of the Co–Sn diffraction pattern using different x give similar C_{ij}, as would be expected, but suggest that larger E_{ij} are needed to obtain these correlations for x near 0.5 than for small or large x. Consistent with this hypothesis, the fitted E_{ij} for the Ni–Sn system were larger positive for the middle x value than the two extrema in 22 out of 34 cases. However, the C_{ij} varied far less consistently. All C_{2j}, C_{31}, and also C_{5j} for even j, increased with x. C_{3j} for even j, C_{5j} for odd j and C_{60} decreased with x. Several of these correlations changed sign across the series. The other values had maxima or minima at intermediate x or stayed nearly constant. Comparison of simulations #7 and #8 for the Co–Ge system showed very different behavior. The high-x simulation had C_{ij} that were in general the same sign but larger in magnitude than those of the low-x simulation, while the E_{ij} were in general of the same sign but smaller for the high-x phase. There is an implication that the changes in the Co–Ge patterns with x are a consequence of interactions becoming generally stronger as the composition approaches $x = 0.5$, whereas there is an additional, complex change in the interactions with composition in the Ni–Sn system.

Effect of Temperature

The only simulations that allowed the effect of annealing temperature to be assessed were the two for $Co_{1.63}Ge$. No consistent pattern of temperature variation was apparent in the C_{ij} values. However, almost all of the fitted E_{ij} energies were larger in magnitude at high temperature. A few E_{5j} and E_{6j} became smaller or changed sign.

Poor Fit for Sample #8

The poor fit obtained for $Co_{1.86}Ge$ (simulation #8) may imply that projection down $[1\bar{1}0]$ did not faithfully represent the three-dimensional structure for this sample. There was an additional diffuse patch of intensity around $(\frac{1}{2}\frac{1}{2}0)$ in the experimental hhl diffraction pattern for this phase (Fig. 1c). Furthermore, an additional set of diffuse streaks, not observed for any of the other samples of this study but similar to those observed in the Fe–Ge system, has been seen in $h0l$ patterns for $Co_{1.86}Ge$ at $\frac{1}{2}0l$ (A.-K. Larsson, unpublished data). It is possible that these two features have a common origin but arise from differently oriented twin lamellae, since the additional patches in the hhl pattern have position vector $[\frac{1}{2}\frac{1}{2}0]^* = [0\,1\,0]^* + [\frac{\bar{1}}{2}\frac{1}{2}0]^*$, and the latter vector is related by $60°$ rotation to $[\frac{1}{2}00]^*$, the position vector of the strongest part of the $h0l$ diffuse streak.

Nature of the "Double-Line" Phase

An important aspect of the modeling strategy used in this study is that it is possible to construct structures corresponding to hypothetical diffraction patterns, analyze their correlations, and find E_{ij} values, if any, which produce them as equilibrium states. This was done for possible diffraction patterns related to the observed for the Ni–Ge system, namely:

(i) A pattern with a single set of diffuse loci at k values intermediate between the two of the actual sample. A 5:3 weighted average was used.

(ii) Modulation wave syntheses and E_{ij} fits were calculated for two single-line patterns with lines corresponding to each of the two in the experimental phase. C_{ij} and E_{ij} were then calculated for a 5:3 "mechanical mixture" of the two.

The correlation and interaction energy data are given in Table 2 for (a–b) the fit to the double line pattern itself, (c–d) single-line case (i), and (e) interaction energies for mechanical mixture case (ii). Averaged C_{ij} values are not given for latter case since they were very similar to those of the double-line pattern (Table 2a).

The majority of E_{ij} and C_{ij} for the double-line pattern and case (i) are very similar. Seven C_{ij} differ by more than 0.5 kT ($ij = 20, 30, 50, 52, 60, 61,$ and 62). All are larger in magnitude for the single-line case but of the same sign as those of the double-line except C_{60} and C_{62}, which differ in sign (along with C_{51} and C_{64}). Two E_{ij} also differ in sign: E_{52} and E_{61}. Another eight differ by more than 0.5 kT between the two data sets. For instance, E_{40} is large and E_{50} small for the double-line fit, whereas the converse is true for the single-line case. Note that all the major differences are for relatively long range correlations and interactions ($i = 4$–6), implying that it is these third-nearest neighbor interactions between A' sites which favor the double-line structure over the single-line structure. This was confirmed by running a Monte Carlo equilibration with the E_{ij} fixed at the value of Table 2b except for $i = 5$–6, which had E_{ij} set to zero. The corresponding real-space array gave a diffraction pattern with large diffuse spots at $l = 0.5$ and 1.5, badly defined lines, and no discernible double line structure (Fig. 8c). The pattern was similar to those of the modulated structures obtained in Ref. (5). The fact that patterns with single sinusoidal loci were (somewhat fortuitously) obtained in that paper shows that second-nearest neighbor interactions alone are sufficient to define single undulations in some cases, but not the double-line structure of the Ni–Ge system.

TABLE 2
C_{ij} and E_{ij} for Simulations Relating to the Double-Line Ni–Ge Sample

(a) C_{ij} for simulation of double-line phase
#9   Ni–Ge $x = 0.70$ cycle 51   rms = 0.0085

	$i = 0$	1	2	3	4	5	6
$C_{ij}, j = 0$		0.93	1.85	− 1.22	− 0.26	0.18	0.48
1	− 0.02	0.20	− 0.20	− 0.25	0.22	0.18	− 0.06
2	1.17	− 0.38	− 0.69	0.60	0.20	− 0.19	− 0.45
3	0.02	− 0.07	0.02	0.08	− 0.09	− 0.10	0.05
4	− 0.56	0.17	0.36	− 0.28	− 0.10	0.08	0.21

(b) E_{ij} for simulation of double-line phase
#9   Ni–Ge $x = 0.70$ cycle 51   rms = 0.0085

	$i = 0$	1	2	3	4	5	6
$E_{ij}, j = 0$		1.78	2.28	− 0.95	0.64	0.17	0.89
1	1.14	1.20	0.14	0.22	0.77	0.90	0.52
2	1.03	0.65	0.27	0.83	0.36	0.48	− 0.14
3	0.71	0.52	0.60	0.44	0.42	0.15	0.10
4	0.49	0.40	0.48	0.28	0.34	0.14	0.11

(c) C_{ij} for single line phase with intermediate $k_0 = 0.354$, $k_1 = 0.261$
Ni–Ge $x = 0.70$ cycle 25   rms = 0.0082

	$i = 0$	1	2	3	4	5	6
$C_{ij}, j = 0$		0.98	2.47	− 2.30	− 0.28	2.02	− 0.75
1	0.03	0.19	− 0.30	− 0.26	0.71	− 0.18	− 0.65
2	1.19	− 0.39	− 0.83	1.06	0.13	− 1.13	0.68
3	0.03	− 0.08	0.07	0.11	− 0.27	0.07	0.36
4	− 0.55	0.18	0.43	− 0.46	− 0.11	0.52	− 0.27

(d) E_{ij} for single line phase
Ni–Ge $x = 0.70$ cycle 25   rms = 0.0082

	$i = 0$	1	2	3	4	5	6
$E_{ij}, j = 0$		1.06	1.53	− 1.76	0.02	1.00	0.41
1	0.83	0.62	0.09	0.36	1.11	0.21	− 0.67
2	0.86	0.37	0.18	0.34	0.34	− 0.17	0.17
3	0.58	0.45	0.32	0.30	0.25	0.27	0.19
4	0.34	0.32	0.34	0.24	0.25	0.08	0.11

(e) E_{ij} for 5:3 mechanical mixture of two single line phases
Ni–Ge $x = 0.70$

	$i = 0$	1	2	3	4	5	6
$E_{ij}, j = 0$		1.99	3.09	− 1.24	0.77	0.62	0.72
1	0.81	1.08	0.14	0.29	0.89	0.98	0.36
2	1.07	0.34	0.21	0.77	0.50	0.23	− 0.04
3	0.66	0.53	0.40	0.52	− 0.27	0.20	0.32
4	0.38	0.52	0.44	0.34	− 0.11	0.20	0.08

When the case (ii) data (Table 2e) and those for the double-line phase (Table 2b) are compared, all C_{ij} values except three, and all E_{ij} except two, are very similar. This prompted the question as to whether "the double-line phase" is homogeneous, or is actually a mosaic of small domains corresponding to each of the two single-line structures. The two single-line structures that were averaged to form the case (ii) data had C_{ij} of the same sign and/or small magnitude for $i \leq 3$, but were distinguishable on the basis of longer range correlations such as C_{40}, C_{42}, C_{44}, C_{50}, and C_{51}, which were of substantial magnitude but opposite sign in the two structures. Therefore, any domains of either structure that were present could be imaged by making a map of sites which had zero, one or two neighbors of the same occupancy at $\pm [4, 0]$ or $\pm [5, 0]$, corresponding to large positive, small and large negative values for the "local average" C_{i0}, respectively. This was done, and the correlation map obtained from the real-space structure of the double-line phase gave an intimate, apparently random intermingling of pixels with 0, 1 or 2 like neighbors. A similar map with the number of like neighbors averaged over 3×3 domains showed that almost all such domains had on average one like and one unlike neighbor per site (rounded to the nearest integer). Sites with different numbers of like neighbors were intermingled on a unit-cell scale, smaller than the scale at which the two single-line structures would be distinguishable. Therefore, the double-line structure obtained from the Monte Carlo routine is better regarded as a single phase than as an intergrowth. The extreme similarity of diffraction patterns and C_{ij} values for this single phase and a mechanical mix of two phases implies that multibody correlations are necessary to distinguish the two. For instance, the single phase will tend to have sites with two like neighbors at $\pm [4, 0]$ in close proximity to sites with two unlike neighbors, while the converse is true when large domains of single-line phases are present. This difference can be expressed using four-body correlations $s_{00}s_{ij}s_{40}s_{(4+i)j}$, where the s are occupancy pseudo-spin variables.

Although it is not possible to prove that the experimental sample was single-phase without data on multibody correlations, we have shown it to be possible that the intricate diffraction pattern observed may be produced by a single phase. Equilibration using a modification of the Monte Carlo routine of Ref. (5), with E_{ij} set to those of Table 2b, showed almost no change in C_{ij} or calculated diffraction pattern from cycle 20 up to cycle 857, implying that the double-line pattern represents true thermodynamic equilibrium for these E_{ij}.

Homogeneity of Simulated Structures

A feature of all the lattice realizations obtained from the Monte Carlo routine that was not observed in the output

from the modulation wave syntheses is that about 4% of the area of the projected lattice was composed of domains of pure end-member composition ($x = 0$ or $x = 1$, depending on which was closest to the average composition). Analysis of the compositional variation of different-sized random samples of the lattice showed that the end-member domains were about 6–12 pixels across (one pixel was $b_{B8}/2 \times c_{B8}/2$). Comparison of the 857-cycle double-line structure with those from shorter run times showed that the domains did not grow or shrink with time. Since these domains were similar in size and concentration for all simulations, they are probably a kinetically inert artifact of the Monte Carlo reordering process, being difficult to remove once formed rather than genuinely stable. Interestingly, the interior portion of only one lattice realization ($Co_{1.86}Ge$, Fig. 6c) showed *visually* discernible domains of Ni_2In type, and this was a relatively poor simulation of an atypical sample. It is likely that most of the inhomogeneity in bulk composition is concentrated around the edges of the 500×500 arrays and is purely a consequence of the finite size of the array used.

Extension to Three Dimensions

Although the energies calculated in this study quantitatively determined (E_{ij}) or described (C_{ij}) the two-dimensional projections of the corresponding occupancy distributions, it is not straightforward to convert them quantitatively into equivalent energies in three dimensions. Each interaction energy is, to a first approximation, the sum of several three-dimensional interaction energies which project onto the same $[i, j]$ vector. Likewise, each C_{ij} is an average of the correlations along each of these vectors. A unique mapping of two-dimensional terms onto the three-dimensional ones may be feasible if the number of independent $[i, j]$ terms in the projection and the number of symmetrically distinct three-dimension terms is equal, and the matrix relating them is nonsingular. In practice, such conditions are never attained for these systems. In the three-dimensional structures, the A' sites are linked to 20 first-nearest neighbors by corner- and face-sharing of their coordination polyhedra (5). The intersite vectors belong to 4 symmetrically distinct types: $\langle 1\,0\,0 \rangle$, $\langle \frac{2}{3}\frac{1}{3}\frac{1}{2} \rangle$, $\langle \frac{2}{3}\frac{4}{3}\frac{1}{2} \rangle$, and $\langle 0\,0\,1 \rangle$ (all indices with respect to the hexagonal $B8$ subcell). In the two-dimensional model, these four types project onto $\langle i, j \rangle = \langle 1, 0 \rangle + \langle 2, 0 \rangle$, $\langle 0, 1 \rangle + \langle 1, 1 \rangle$, $\langle 0, 1 \rangle + \langle 2, 1 \rangle$, and $\langle 0, 2 \rangle$, respectively—a total of 6 distinct species of $\langle i, j \rangle$ (indexed on the $a/2 \times c/2$ rectangular net). The number of symmetrically distinct $\langle i, j \rangle$ species remains larger than that of three-dimensional $\langle u, v, w \rangle$ when second-nearest neighbors and third-nearest neighbors are considered (the relative numbers are 16:12 and 30:26, respectively). This is a consequence of the large number of neighbors, combined with the low symmetry of the two-dimensional projection relative to that of the three-dimensional average structure. Some con-

straints on three-dimensional correlations could be obtained by least-square fitting in principle, although correlations between them would limit the possibility of obtaining precise values.

The large number of $\langle u, v, w \rangle$ interneighbor vectors to be considered, and their high multiplicity, imply that a full three-dimensional model would be three orders of magnitude more computationally intensive than the current simulations, and hence not practical at the present time. However, characterization of a three-dimensional model using a cluster approach may be a viable direction for future work.

Absence of the Hexad Axis in 2-D Simulation

The loss of hexagonal symmetry in projection does not have much adverse effect on the faithfulness of the simulations in this study ($Co_{1.86}Ge$ appears to be an exception). The A' sublattice contains many triplets of sites that are connected in a triangular fashion. Repulsive interactions between like occupancies necessarily lead to frustration of ordering schemes in such a topology. In particular, ordering schemes that are a response to repulsive interactions do not in general maintain the hexagonal symmetry of the interactions. A preliminary study has been done of ordering in a hexagonal net like the (001) plane of the compounds of this study. The combination of repulsive $\langle 1, 0 \rangle$ and $\langle 2, 0 \rangle$ interactions and attractive $\langle 1, \bar{1} \rangle$ interactions (all ± 2 kT in magnitude) was found to be sufficient to generate large nonhexagonal domains. For composition $x = 0.3$, there was a tendency to form zigzag chains of occupied or vacant sites, defining a unique $[1\bar{1}0]$ direction, as observed in the experimental systems. Locally hexagonal domains were also seen with honeycomb ordering. A portion of the lattice realization illustrating these phenomena is shown in Fig. 9.

CONCLUSIONS

For each of the experimental electron diffraction patterns, we have obtained by modulation wave synthesis a real-space distribution which gives a similar diffraction pattern. Good fits obtained using a Monte Carlo routine suggest that all these structures can be produced by two-body interactions and are minimum-energy structures for appropriate sets of interaction energies E_{ij}.

The fitted interaction energies, and the correlations C_{ij} which describe the structure, vary with the system, the composition x, and the annealing temperature of the sample.

In summary, we conclude that there exist sets of two-point interaction energies E_{ij} for which any of the observed diffraction patterns can correspond to stable structures. All the observed patterns can be produced by single phases. Small domains of A_2B or AB stoichiometry that are statistically
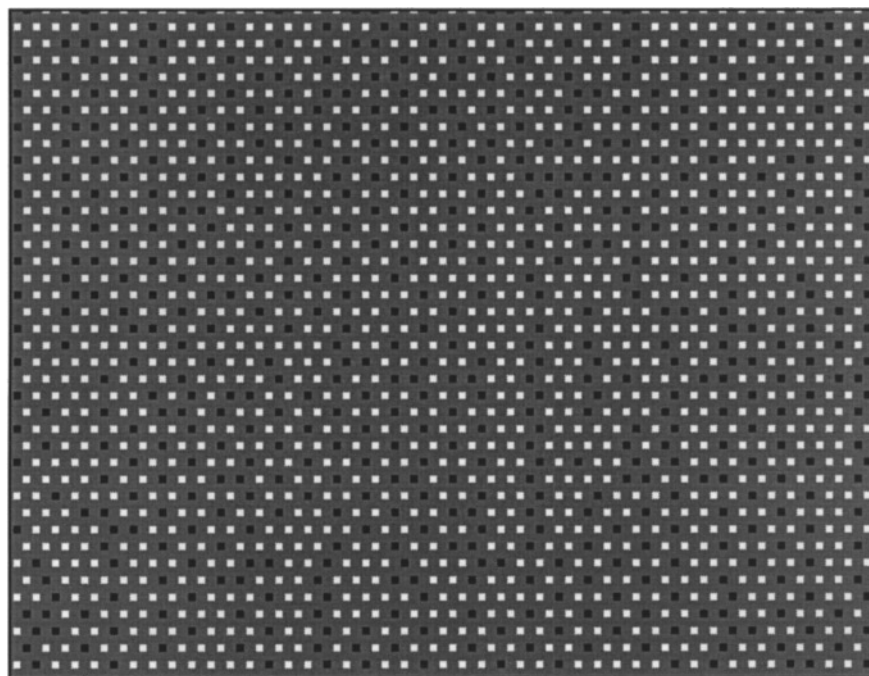
FIG. 9. Spontaneous breaking of hexagonal symmetry in the $(001)_{B8}$ plane due to mutual frustration of repulsions. Note ordering of vacant and occupied sites into vertical strips parallel to a preferred $[1\bar{1}0]$ direction. Interaction energies were $+2$, -2, and $+2$ kT along $\langle 100 \rangle$, $\langle 1\bar{1}0 \rangle$, and $\langle 200 \rangle$ vector sets, respectively. Composition was $x = 0.3$.

detectable in the fitted lattice realizations are likely to be kinetically persistent nonequilibrium features or edge effects. The observed sinusoidal lines in reciprocal space arise because the interaction energies couple so as to produce relatively poor correlations along **c** (particularly C_{01} and C_{03}) but strong correlations both perpendicular and oblique to **c**. In the case of the double-line patterns from the Ni–Ge system, significant magnitudes for interaction energies with $i = 5$–6 are essential to produce the observed patterns. These correspond to third-nearest neighbor interactions between A' sites in the structure. In the Ni–Ge system, such terms destabilize single-curve diffraction patterns at the usual k values, and give rise to patterns with two nearly parallel curves at higher and lower k.

The large number of nearest neighbors, significant magnitude of interactions out to second- and third-nearest neighbors, and particularly frustration due to the triangular interconnection pattern and repulsive nature of most interaction energy terms are all responsible for the failure of these phases to form conventional commensurate or incommensurate modulated superstructures. In three dimensions, the interactions may well show the hexagonal symmetry of the sublattice, even though frustrated repulsion leads to breaking of this symmetry in the resulting local ordering schemes. The sinusoidal-locus structures are potential equilibrium states for appropriate sets of two body interaction energies and may be regarded as a distinct state between

conventional modulated structures giving spot diffraction patterns on the one hand, and full disorder on the other, equating with the "transition state" of van Dyck *et al.* (15).

REFERENCES

1. A.-K. Larsson, "Crystal Structures of Tin Intermetallics; Honeycomb Nets, Superstructures and Edshammar Polyhedra." Ph.D. thesis, Univ. of Lund, Sweden, 1994.
2. A.-K. Larsson, L. Stenberg, and S. Lidin, *Acta Crystallogr. B* **50,** 636 (1994).
3. S. Lidin and A.-K. Larsson, *J. Solid State Chem.* **118,** 313 (1995).
4. A.-K. Larsson and R. L. Withers, *J. Alloys Compd.* **264,** 125 (1998).
5. A. G. Christy and A.-K. Larsson, *J. Solid State Chem.* **135,** 269 (1998).
6. A.-K. Larsson, R. L. Withers, and L. Stenberg, *J. Solid State Chem.* **127,** 222 (1996).
7. B. E. Warren, B. L. Averbach, and B. W. Roberts, *J. Appl. Phys.* **22,** 1493 (1951).
8. J. M. Cowley, *Acta Crystallogr. A* **24,** 557 (1968).

9. P. A. Flinn, *Phys. Rev.* **104,** 350 (1956).

10. T. R. Welberry, *J. Appl. Crystallogr.* **19,** 382 (1986).

11. T. R. Welberry and R. L. Withers, *J. Appl. Crystallogr.* **20,** 280 (1987).

12. T. R. Welberry and B. D. Butler, *J. Appl Crystallogr.* **27,** 205 (1994).

13. T. R. Welberry, R. L. Withers, and S. C. Mayo, *J. Solid State Chem.* **115,** 43 (1995).

14. T. R. Welberry and R. L. Withers, *J. Appl Crystallogr.* **24,** 18 (1991).

15. D. van Dyck, R. de Ridder, and S. Amelickx, *Phys. Status Solidi. A* **59,** 513 (1980).

16. R. de Ridder, D. van Dyck, and S. Amelickx, *Phys. Status Solidi. A* **61,** 231 (1980).

17. B. D. Butler and T. R. Welberry, *J. Appl. Crystallogr.* **25,** 391 (1992).

18. M. Ellner, *J. Less-Common Met.* **48,** 21 (1976).

19. H. Fjellvåg and A. Kjekshys, *Acta Chem. Scand. A* **40,** 23 (1986).

20. A. M. Stoneham and P. J. Durham, *J. Phys. Chem. Solids* **34,** 2127 (1973).

21. E. Iguchi and R. J. D. Tilley, *Phil. Trans. Roy. Soc. A* **286,** 55 (1977).

22. Christy, A. G., *Phys. Chem. Minerals* **16,** 343 (1989).